Article
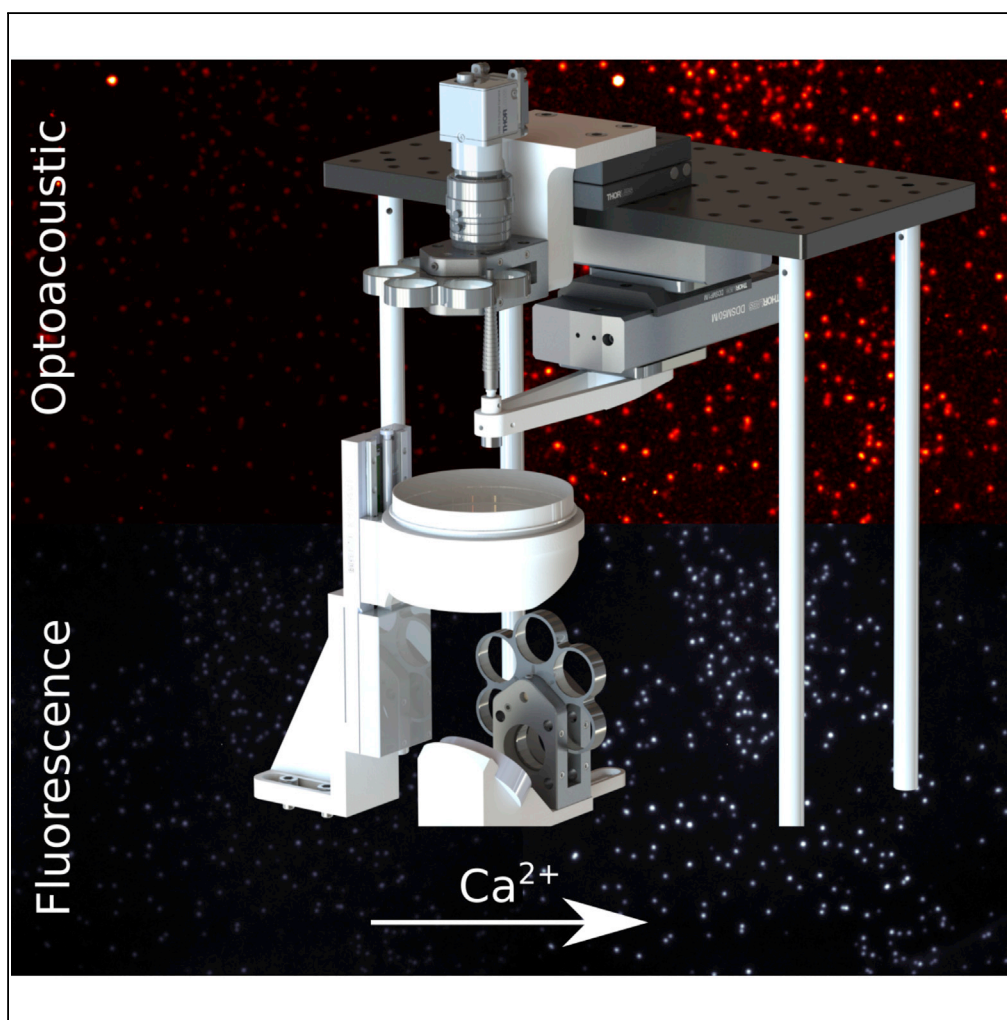
High-Throughput Platform for Optoacoustic Probing of Genetically Encoded Calcium Ion Indicators

Urs A.T. Hofmann,
Arne Fabritius,
Johannes Rebling,
Héctor Estrada, X.
Luís Deán-Ben,
Oliver Griesbeck,
Daniel Razansky

daniel.razansky@uzh.ch

HIGHLIGHTS
New platform for rapid
screening of optoacoustic
calcium ion indicators

Coregistered
fluorescence and
optoacoustic recordings
from bacterial colonies

Sensitive imaging and
selective probing in
calcium-loaded and
calcium-unloaded states

Assessment of protein
photobleaching
resistance to pulsed laser
irradiation

Article

High-Throughput Platform for Optoacoustic Probing of Genetically Encoded Calcium Ion Indicators

Urs A.T. Hofmann,[1,2] Arne Fabritius,[3] Johannes Rebling,[1,2] Héctor Estrada,[1,2] X. Luís Deán-Ben,[1,2] Oliver Griesbeck,[3] and Daniel Razansky[1,2,4,*]

SUMMARY

Functional optoacoustic (OA) imaging assisted with genetically encoded calcium ion indicators (GECIs) holds promise for imaging large-scale neuronal activity at depths and spatiotemporal resolutions not attainable with existing optical microscopic techniques. However, currently available GECIs optimized for fluorescence (FL) imaging lack sufficient contrast for OA imaging and respond at wavelengths having limited penetration into the mammalian brain. Here we present an imaging platform capable of rapid assessment and cross-validation between OA and FL responses of sensor proteins expressed in *Escherichia coli* colonies. The screening system features optimized pulsed light excitation combined with ultrasensitive ultrasound detection to mitigate photobleaching while further allowing the dynamic characterization of calcium ion responses with millisecond precision. Targeted probing of up to six individual colonies per second in both calcium-loaded and calcium-unloaded states was possible with the system. The new platform greatly facilitates optimization of absorption-based labels, thus setting the stage for directed evolution of OA GECIs.

INTRODUCTION

Functional, volumetric, and non-invasive imaging of large neuronal populations at high spatiotemporal resolution is essential for expanding our understanding of complex brain functions (Ji et al., 2016; Prevedel et al., 2014). Fluorescence (FL) microscopy assisted with genetically encoded calcium ion indicators (GECIs) has facilitated the direct visualization of neuronal activation beyond traditional macroscopic observations looking at hemodynamic changes as indirect manifestation of neural activity (Kannan et al., 2018). State-of-the-art techniques such as multiphoton excitation fluorescence imaging have enabled the mapping of fast neuronal activation with sub-cellular resolution at hundreds of micrometers depths in the scattering brain of rodents (Chamberland et al., 2017). Extensive efforts are being directed toward optimizing quantum yield (σ), molar extinction coefficient (ε), kinetics, and photostability of GECIs as well as other calcium ion (Ca^{2+}) and voltage sensors (Thestrup et al., 2014; Chen et al., 2013; Mank et al., 2006; Shen et al., 2018). Yet, intense light scattering in the brain, skin, and skull restricts optical microscopy to highly invasive observations at sub-millimeter depths and fields of view (FOVs) while imposing additional limitations on the effective spatiotemporal resolution due to the need for beam scanning (Helmchen and Denk, 2005; Mittmann et al., 2011; Stirman et al., 2016). Optoacoustic (OA) imaging overcomes the optical diffusion barrier and hence bridges the gap between microscopic and macroscopic realms (Deán-Ben et al., 2017; Wang, 2009). Being based on optical-absorption contrast, OA methods uniquely enable multi-scale imaging of hemodynamic responses across entire mammalian brains at several millimeters' depth (Ni et al., 2018; Gottschalk et al., 2016; Wang et al., 2003; Yao et al., 2015). More importantly, OA has recently been shown to be sensitive to Ca^{2+} and voltage signaling *in vivo* (Deán-Ben et al., 2016; Rao et al., 2017; Zhang et al., 2017; Gottschalk et al., 2019). This unique contrast versatility of OA imaging, combined with its high temporal resolution and large scalability, is poised to advance our understanding of neuronal activity and mechanisms of neurovascular coupling in the whole rodent brain (Deán-Ben et al., 2017).

Existing GECIs and genetically encoded voltage indicators (GEVIs) are, however, sub-optimal for OA imaging because most biosensors used to visualize neuronal activity have been specifically optimized for FL imaging (Laufer et al., 2013). For instance, strong variations in σ may not result in detectable OA responses (Weber et al., 2016). Generally, proteins with low σ have improved OA responses and have been shown to be more photostable (Laufer et al., 2013). Sensors responding to Ca^{2+} changes by strong

[1]Institute of Pharmacology and Toxicology and Faculty of Medicine, University of Zurich, Winterthurerstrasse 190, 8057 Zurich, Switzerland

[2]Institute for Biomedical Engineering and Department of Information Technology and Electrical Engineering, ETH Zurich, Gloriastrasse 35, 8092 Zurich, Switzerland

[3]Tools for Bio-Imaging, Max Planck Institute, Am Klopferspitz 18, 82152 Martinsried, Germany

[4]Lead Contact

*Correspondence: daniel.razansky@uzh.ch

corresponding changes in their ε are available, holding promise for OA neuroimaging applications (Shen et al., 2018; Zhao et al., 2011). Particularly, green fluorescent protein-derived GCaMP sensors have been shown to provide sufficient OA signal changes to be detectable in highly vascularized mammalian brains (Gottschalk et al., 2019). Red fluorescent genetically encoded Ca^{2+} indicators for optical imaging (R-GECO) exhibit similar changes in ε when bound to Ca^{2+} while having excitation and emission spectra in a wavelength range where scattering and auto-fluorescence tissue background is diminished (Shen et al., 2018). Yet, an optimal sensor for OA Ca^{2+} imaging would feature strong fractional absorbance changes in response to Ca^{2+} variations and have its peak absorption in the far-red or near-infrared spectral range where the blood absorption background also is diminished. However, currently available protein screening platforms, e.g., employing directed evolution approaches, are tailored toward optimization of FL imaging performance, making them unsuitable for screening the optimal variants for OA (absorption-based) imaging.

Herein, we present an imaging and screening platform for efficient characterization of changes in both OA and FL signal intensity upon Ca^{2+} delivery and showcase its performance for high-throughput screening of a large number of *Escherichia coli* (*E. coli*) bacterial colonies expressing R-GECO1 proteins. The system thus enables optimization of sensor's σ, ε, and photostability and can readily be adapted to other genetically encoded biosensors.

RESULTS

The Rapid Protein Probing Platform

The developed hybrid imaging platform allows for a rapid screening of both OA and FL properties of several hundred *E. coli* colonies growing on a Petri dish and expressing genetically encoded protein variants (Figure 1). In a mechanical overfly scan mode, OA imaging is performed over the entire 50 mm × 50 mm FOV with a uniform step size of 100 μm, which takes about 150 s (line scan rate of 3.34 Hz). The pulse repetition frequency (PRF) of the excitation laser reaches 5 kHz when the stages reach their maximum velocity of 500 mm s^{-1} during the scan. Oversampling is avoided at acceleration and deceleration phases by using position-dependent triggering of the laser source (see Transparent Methods for details). Band-pass frequency filtering and envelope extraction of the acquired datasets were performed during the scan, allowing for line-by-line live preview of the acquired image data.

For a more subtle protein characterization, positions of all the colonies are first mapped using either an overfly OA scan or an FL wide-field image and colonies are subsequently probed individually in the OA mode. This further allows to increase screening speed, diminish bleaching effects, and/or enable signal averaging. In our first experiments, over 95% of the colonies were accurately localized with 100 μm precision from the FL image by applying a circle detection algorithm (Figure 2A, see Methods for details). Time required to travel between individual colonies was subsequently calculated taking into account stage accelerations and maximum velocities (Figure 2B). The so-called traveling salesman problem was solved to determine the optimal colony probing path using a genetic algorithm (Figure 2C, see Transparent Methods for details) (Beardwood et al., 1959). Example of an optimized path for visiting 483 colonies is shown in Figure 2D. An average probing speed of 6 colonies per second was attained when accounting for probing, data acquisition, and hardware interfacing.

Optoacoustic and Fluorescence Probing of GECIs

Owing to its distinct absorption spectrum and high sensitivity to Ca^{2+} dynamics, R-GECO1 was selected for testing signal to noise ratio (SNR), imaging speed, and Ca^{2+} delivery protocol attained by the developed platform (calculated OA and FL properties of alternative GECIs are enlisted in Table S1). Note that the cell colonies are not visible with the naked eye in both loaded and unloaded states (Figure 3A), underlining the required high sensitivity of the OA probing platform. The OA spectrum of the purified protein correlates well with the optical absorption spectrum measured in a wavelength range between 430 nm and 680 nm (Figure 3B). High relative changes in OA and FL signals were observed when the protein binds to Ca^{2+}, indicating that the sensor is suitable for both modalities. The strong changes in OA spectra further indicate that ε is substantially altered due to Ca^{2+} binding, which is consistent with the observed strong changes in the optical absorption spectrum. Specifically, below an excitation wavelength of 475 nm, a moderate decrease in OA signal is observed following Ca^{2+} delivery (−33% on average). The OA signal reaches its maximum intensity near the optical excitation peak of R-GECO1 (577 nm/561 nm for Ca^{2+} unbound/bound states, respectively). For 560 nm excitation wavelength, Ca^{2+} delivery has boosted the OA signal intensity
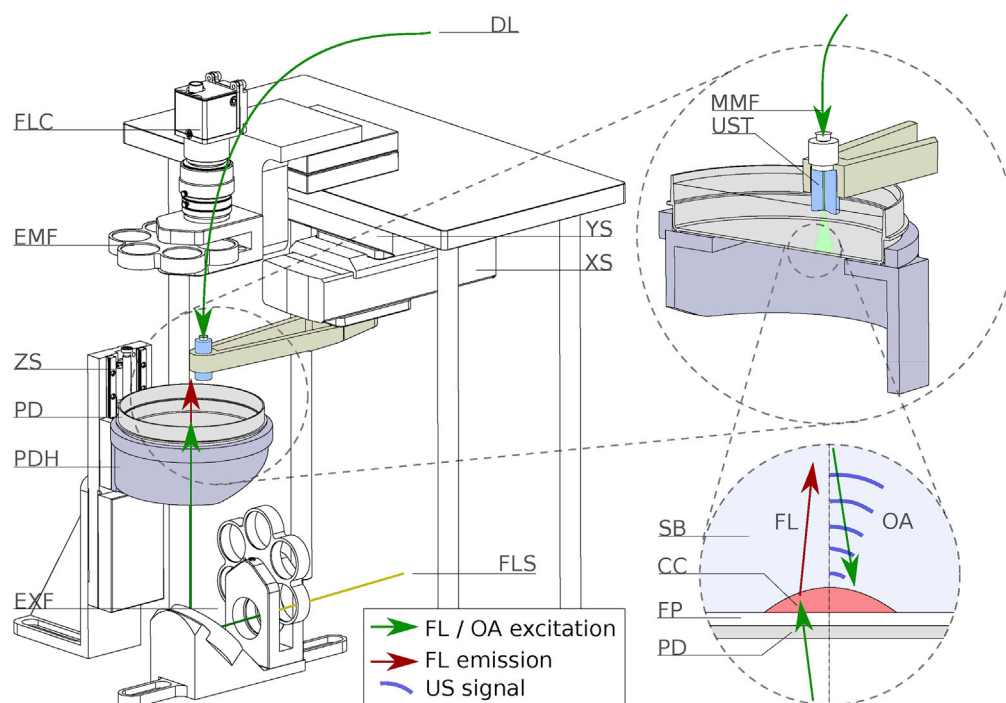
Figure 1. Combined OA and FL Screening Platform for Ca^{2+} Biosensors

A Petri dish (PD) positioned in a holder (PDH) contains cell colonies (CC) on a filter paper (FP) immersed in screening buffer (SB) for acoustic coupling. A motorized z-stage (ZS) is used to switch between OA and FL imaging modes. In the OA mode, an FOV of 50 mm × 50 mm is rapidly acquired by scanning an US transducer (UST) over the PD using two perpendicularly mounted stages (XS, YS). A multimode fiber (MMF) delivers laser pulses from a dye laser (DL), tuned to the required wavelength for OA excitation, through an opening in the transducer's active aperture. FL imaging is performed with a camera (FLC) equipped with an emission filter (EMF) whose FOV matches the size of the Petri dish. For imaging, the platform is lowered by 30 mm and the transducer is moved out of the camera's FOV. For uniform concentric illumination, excitation light was provided by a tungsten light source from below (FLS) equipped with the appropriate excitation filter (EXF) for the tested protein.

by 201% relatively to the Ca^{2+}-free baseline value, comparable to the signal increase in the optical absorption spectra. The protein did not bleach significantly over 50 measurement cycles.

OA and FL images of 500–800 individual R-GECO1-expressing colonies positioned in a single Petri dish were subsequently acquired before and after Ca^{2+} delivery (Figures 3D–3G) according to the workflow depicted in Figure 3C. Sufficiently strong OA signals from single laser shots (SNR >20 dB) were generated by per-pulse-energies (PPEs) as low as 25 μJ (6.54 mJ cm^{-2}). The increase in OA and FL signal intensity correlated with R^2 = 0.38 (Figure 3G). *E. coli* colonies expressing R-GECO1 showed a strong increase in OA signal following Ca^{2+} delivery by approximately 305% compared with Ca^{2+}-free baseline value, whereas the FL signals increased by approximately 270% compared with the baseline value after Ca^{2+} delivery (Figures 3H and 3I). The lower signal enhancement in FL mode can be attributed to higher background autofluorescence signal of flavins (Mihalcescu et al., 2015). Control plates were imaged before and after adding 3-(N-morpholino)propanesulfonic acid (MOPS) buffer instead of Ca^{2+}-enriched MOPS buffer to evaluate the influence of photoactivation effects. The latter were previously reported to lead to approximately 20% FL signal increase for the K-GECO1 sensor at 405 nm and 488 nm after light fluence deposition of 1.76 J cm^{-2} and 6.12 J cm^{-2}, respectively (Shen et al., 2018). The FL signal of the control plate slightly increased by 24%, whereas an opposite effect was observed in the OA mode. This finding indicates slight photoactivation of the protein during the first OA scan, which was performed between the first and second FL image acquisition. During the second OA scan, bleaching effects have dominated the photoactivation, leading to an overall 24% decrease in OA signal intensity (Figures 3H and 4A).

To showcase the platform's capability to distinguish between different proteins, we further imaged K-GECO1 (Shen et al., 2018) and RCaMP1.07 (Ohkura et al., 2012) expressing colonies. OA signal increases
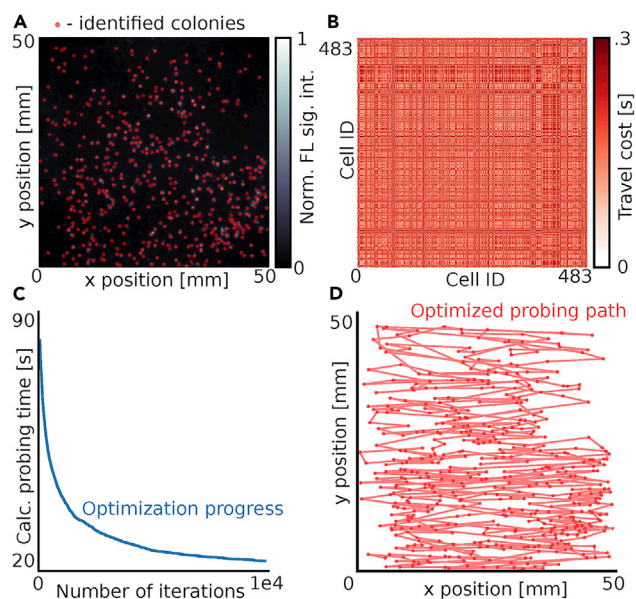
Figure 2. Path Optimization Method for Fast OA Probing of Cell Colonies in a Petri Dish

(A) Before selective OA probing, an FL image of the entire Petri dish is acquired to identify the location of the colonies based on their autofluorescence or Ca^{2+}-mediated signal.

(B) Time required to travel between individual cell colonies is calculated taking the stage acceleration and its maximum velocity into account.

(C) The probing order is optimized using iterative genetic optimization algorithm, e.g., resulting in a theoretical travel time of only 21 s for visiting 483 colonies. Note that data acquisition, hardware communication, laser triggering, and post-processing add an overhead to the actual probing times.

(D) Example of the optimized scanning path.

upon Ca^{2+} were measured to be 3.1% and 21.1% respectively, i.e., nearly one order of magnitude lower responses compared with R-GECO1. The difference between theoretically calculated values and experimentally measured signals can be ascribed to a lower resistance of K-GECO1 and RCaMP1.07 to photobleaching (Shen et al., 2018).

To provide stronger evidence for the cell culture viability following OA screening, a plate containing R-GECO1-expressing *E. coli* colonies was additionally imaged at a high PPE (50μJ, 560 nm). The colony providing highest OA signal was subsequently picked, mechanically resuspended, and transferred to a fresh plate. After overnight incubation, visual inspection clearly revealed the expected growth, showcasing cell survival after the screening procedure.

Photobleaching Effects due to Probing

The photobleaching characteristics of R-GECO1-expressing cell colonies were evaluated dynamically using the same platform. Cell colonies were exposed to pulsed laser radiation while OA signal intensity was measured as a function of the deposited energy (Figure 4A). Bleaching experiments were performed at three different PPE levels, namely, 25, 34, and 44 μJ (see inset in Figure 4A), corresponding to 250–450 mJ cm^{-2} cumulative laser energy density reaching the cells. Note that the bleaching affects other background chromophores besides the proteins, which results in a complex photobleaching pattern contributed by multiple fluorescent and absorbing structures each having four possible states, namely, higher-energy excited singlet state S^*, lower-energy singlet state S, excited triplet state T^*, and bleached State X (Gangola and Rosen, 1987). To distinguish between bleaching of cell compartments and Ca^{2+} sensor, measurements were performed at both high and low Ca^{2+} concentrations (solid and dashed lines in Figure 4A, respectively). Although bleaching of background structures is independent of Ca^{2+} concentration and therefore identical in both cases, the protein in the Ca^{2+}-loaded state exhibits a higher absorption coefficient, leading to an increased probability for molecules to be pumped into S^* (proportional to the OA signal intensity). Therefore, initial signal intensities were higher for all Ca^{2+}-loaded cases when compared with their Ca^{2+}-unloaded counterparts. Furthermore, the proteins can transition into the
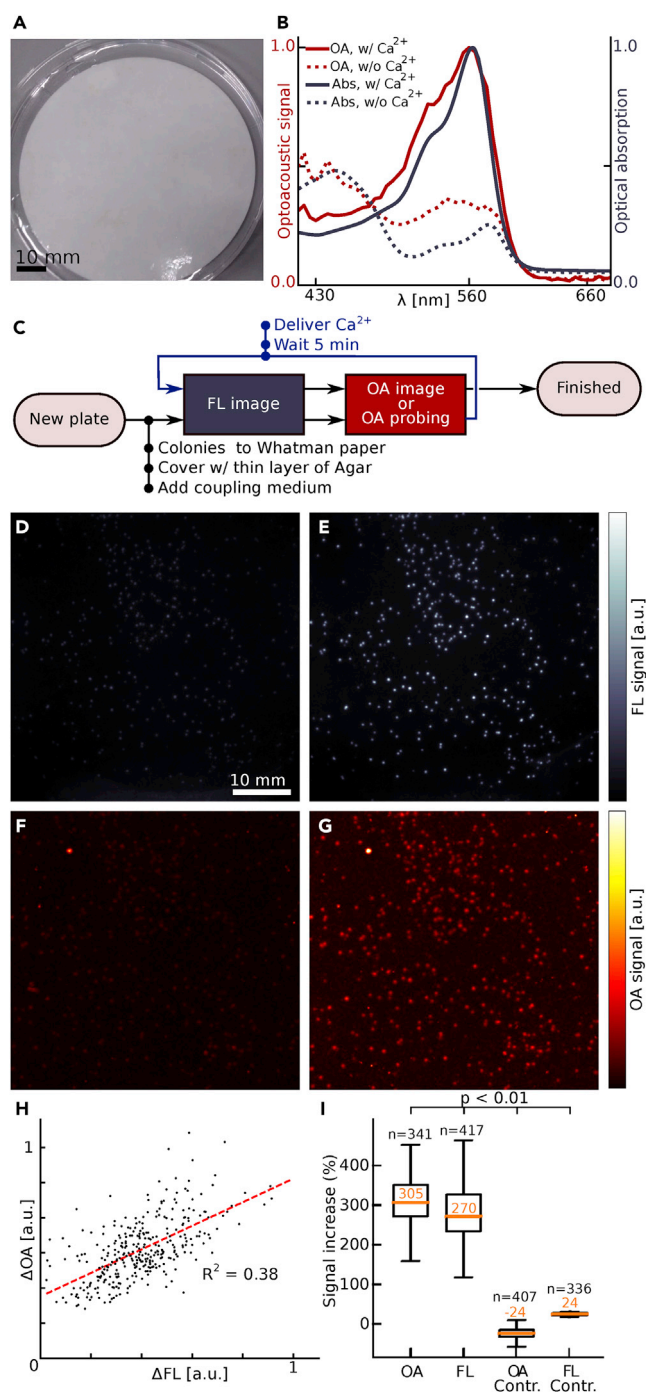
**Figure 3. OA and FL Probing of R-GECO1 Protein**

(A) Photograph of a Petri dish containing a filter paper with *E. coli* colonies expressing R-GECO1.

(B) The optical absorption and OA spectra of the purified protein R-GECO1 were analyzed in Ca^{2+}-unloaded and Ca^{2+}-loaded states.

(C–G) (C) Screening workflow using hybrid OA and FL imaging platform. (D and E) FL image of the colonies before and after Ca^{2+} loading, respectively. The corresponding OA images before and after Ca^{2+} loading are shown in (F) and (G), respectively.

(H) The correlation between signal increase in the FL and OA modes was analyzed for each individual colony, revealing a relatively low value of $R^2 = 0.38$.

(I) The average OA signal increase after Ca^{2+} delivery (305%) was significantly higher than the corresponding FL value ($p < 0.001$, 270%). No significant signal variations were recorded in the control group containing no protein.
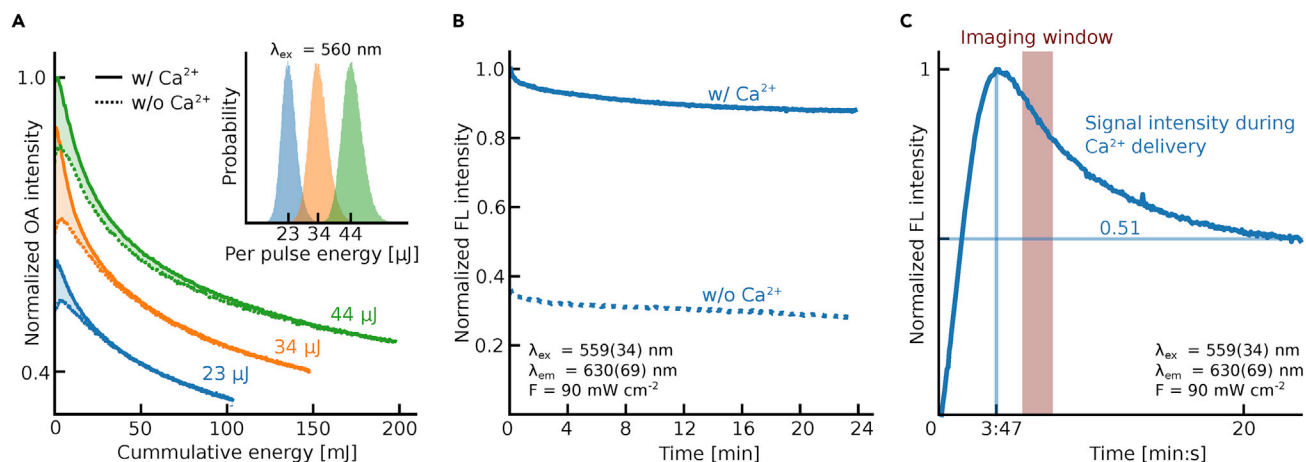
Figure 4. Dynamic Monitoring of Cell Properties in OA and FL Modes

(A) Photobleaching characteristics of R-GECO1 in OA probing mode when colonies are iteratively exposed to pulsed laser radiation. To distinguish between bleaching of background biochromes and Ca^{2+}-sensitive protein, experiments were performed in Ca^{2+}-loaded (solid curves) and Ca^{2+}-unloaded (dashed curves) states. Each measurement represents an average of 30 probed colonies. The inset shows histograms of the PPEs measured by the photodiode at the three used energy levels.

(B) The corresponding photobleaching effects in FL imaging mode using continuous-wave excitation light.

(C) The FL signal continuously monitored after delivering Ca^{2+} to the cells at t = 0 min: following strong increase in the signal intensity after approximately 4 min, the signal decays toward an equilibrium state after approximately 20 min. The excitation light intensity was the same as for the FL bleaching experiments. The time window used for screening is highlighted in red.

bleached state X from either $S*$ or the excited triplet state $T*$, which occurs significantly faster for the Ca^{2+}-loaded case. Owing to increasing size of X and a constant overall population size ($S + S* + T* + X$ = const.), S and $S*$ are decaying faster, leading to a faster decrease in signal intensity for the Ca^{2+}-loaded state. A maximum signal decrease of 55% was observed for the Ca^{2+}-loaded state at PPEs of 44 μJ.

Photobleaching in FL mode was investigated by exposing the entire Petri dish to an unfocused continuous-wave excitation light source with cumulative energy density of 88–177mJ cm^{-2} deposited onto the cells. The FL signal decreased by 10% and 12% at high and low Ca^{2+} concentrations, respectively, after 25 min exposure time (Figure 4B).

Calcium Ion Delivery Dynamics

During Ca^{2+} delivery, the FL signal reaches its peak intensity after 227 s, and then decays by 49% (Figure 4C). As the protein is restricted to the intracellular space, FL and OA signal intensities are directly correlated to Ca^{2+} concentration within the bacteria. It is likely that adding Ca^{2+} to the buffer medium leads to an initial high uptake of the bacteria before it is actively transported out of the cell interior. The Ca^{2+} uptake dynamics are furthermore affected by the time bacteria are stored out of fridge before screening (Figure S1). To avoid unwanted influences of ion uptake dynamics, all experiments were carefully time controlled. Plates were taken from a 7° fridge and imaged immediately (t = 0 min), Ca^{2+} was delivered at t = 5 min, and plates were imaged again at t = 10 min.

DISCUSSION

We developed an imaging platform for combined and co-registered evaluation of key OA and FL excitation parameters of proteins expressed in bacterial colonies. The system can characterize different parameters dynamically without the need for protein purification or special treatment, i.e., by observing cells embedded in a Petri dish directly. We showcased the platform's functionality using Ca^{2+} delivery in R-GECO1-expressing *E. coli*.

OA properties of bacterial cell colonies distributed over an area of up to 50 mm × 50 mm, i.e., the approximate size of a standard Petri dish, can be characterized within less than 3 min by performing a mechanical

overfly scan. In addition, rapid targeted OA probing of individual colonies was performed to extract important protein characteristics, including bleaching and Ca^{2+} delivery dynamics.

The use of a fast, wavelength-tunable dye laser for OA excitation increases probing and imaging speed of this setup by several orders of magnitude compared with previously reported design using optical parametric oscillator lasers (Li et al., 2016). Although mirror-based OA microscopy scanners can image at higher speeds, their effective FOV is diminished due to a highly non-uniform sensitivity field of an ultrasound (US) detector remaining in a constant position (Allen et al., 2018). In contrast, our mechanical scanning approach allowed for attaining uniform sensitivity field in detecting the generated US signals over large FOVs, an ideal trait for high-throughput protein screening.

High-power lasers often employed in OA tomography applications are known for their strong protein bleaching characteristics, thus making photostability an important criterion when developing biosensors for OA imaging (Gottschalk et al., 2015). Using a highly sensitive, focused US sensor in combination with an optimized OA excitation scheme significantly decreased laser exposure and thus bleaching effects while boosting the screening throughput. Yet, OA imaging induced more significant photobleaching in the probed colonies when compared with FL imaging owing to the use of high-peak-power nanosecond-duration laser pulses for OA excitation (Gottschalk et al., 2015). The overall deposited energy in our experiments was 2–3 times higher for the OA mode. In addition, accurate assessment of the bleaching effects caused by nanosecond laser pulses was facilitated by means of the targeted probing mode.

R-GECO1 exhibited a strong increase in its signal intensity following Ca^{2+} delivery in both FL and OA modes. The background signal induced by the intrinsic cell structures was significantly lower in the OA mode leading to better contrast for Ca^{2+} concentration. However, in an early stage of the protein screening process, the OA signal intensity might be insufficient to accurately extract OA properties of all the colonies from an overfly scan. In this case, imaging autofluorescence of bacterial cell compartments in FL mode allows for an accurate identification of colonies even if the protein is in its inactive state. After localizing the colonies based on the FL image, individual OA probing can be facilitated by means of signal averaging to increase the SNR and compare between colonies expressing mutant protein variants.

The current study focused on screening of Ca^{2+}-sensitive proteins in *E. coli* colonies, which were previously shown as a robust platform for directed evolution purposes (Fabritius et al., 2018). Nevertheless, additional applications can be envisioned, such as screening proteins for their dopamine responses (Patriarchi et al., 2018; Sun et al., 2018), using a different cell substrate, optimizing OA signal of chromoproteins, or study the effects of nanobioconjugates influencing Ca^{2+} uptake using OA (Lyu et al., 2016). However, the current sensitivity and spatial resolution of the US detector are not suitable for resolving or sensing individual cells. Our screening platform can seamlessly be operated in a pulse-echo US mode (Estrada et al., 2014), and thus can be potentially employed for screening bacteria containing gas vesicles using its pulse-echo imaging capability (Bourdeau et al., 2018).

OA imaging has the unique capacity to map a large number of hemodynamic parameters using endogenous tissue contrast, such as the dynamic distribution of oxygenated and deoxygenated hemoglobin or the total blood volume (Rebling et al., 2018; Wang, 2009; Yao et al., 2015), and hence offers a more versatile contrast when compared with other neuroimaging techniques (Gozzi and Schwarz, 2016; Jonckers et al., 2011). However, optical absorption of most neuronal activity sensors peaks in the visible light range, limiting their *in vivo* applicability to shallow depths owing to the high absorption by blood in highly vascularized mammalian tissues at those wavelengths. The development of efficient far-red- and near-infrared-shifted sensors using the newly developed protein screening platform can thus open new vistas for the study of neuronal function and neurovascular coupling in whole mammalian brains, a long-standing goal of neuroscience.

In this work, simultaneous probing of both OA and FL properties of proteins expressed in *E. coli* colonies was demonstrated with our method. However, the approach can generally be applied for screening GECIs or other proteins featuring sensing or contrast modulation properties (Patriarchi et al., 2018; Zhao et al., 2011; Shen et al., 2018). For these and other proteins, optimization of maximum OA signal intensity, relative signal change, and protein dynamics are essential to take full advantage of their sensing capacities.

The devised system is therefore expected to facilitate the development of a new generation of sensors optimized for a variety of contrast-enhanced OA imaging applications using directed evolution of gene reporter proteins.

Limitations of the Study

The presented platform is optimized for screening proteins in bacterial colonies allowing for a high throughput and robust handling. In this setting, functionality of the optimized variants needs to be validated in mammalian cell cultures followed by *in vivo* validation.

In our current proof-of-concept experiments, the sensors employed were not yet optimized for OA imaging performance, thus exhibiting low SNR. As a result, relatively high laser intensities were necessary, leading to partial photobleaching. Optimization and comparison between different proteins should therefore rely on their combined OA and photobleaching characteristics.

In our previously published work we have shown the ability to automatically pick bacterial colonies from the dish based on their fluorescent properties (Fabritius et al., 2018). This capacity has not yet been implemented in the newly developed OA screening platform.

METHODS

All methods can be found in the accompanying Transparent Methods supplemental file.

DATA AND CODE AVAILABILITY

The software used for postprocessing and hardware control is available online at https://github.com/razanskylab/. Data are available upon request.

SUPPLEMENTAL INFORMATION

Supplemental Information can be found online at https://doi.org/10.1016/j.isci.2019.11.034.

AUTHOR CONTRIBUTIONS

D.R. and O.G. conceived the study. U.A.T.H. developed and built the screening platform, performed the experiments, and evaluated the datasets. A.F. prepared the Petri dishes, developed the protocol for calcium ion delivery, extracted the purified protein, and measured the optical absorption spectrum. H.E., J.R., and D.R. took part in designing the screening platform. H.E. helped conducting the experiments. X.L.D.-B. measured the OA spectrum of the purified protein. H.E., O.G., and D.R. supervised the research. All authors took part in writing and proofreading the final manuscript.

DECLARATION OF INTERESTS

The authors declare no competing interests.

REFERENCES

Allen, T.J., Spurrell, J., Berendt, M.O., Ogunlade, O., Alam, S.U., Zhang, E.Z., Richardson, D.J., and Beard, P.C. (2018). Ultrafast laser-scanning optical resolution photoacoustic microscopy at up to 2 million A-lines per second. J. Biomed. Opt. 23, 1.

Beardwood, J., Halton, J.H., and Hammersley, J.M. (1959). The shortest path through many points. Math. Proc. Camb. Philos. Soc 55, 299–327.

Bourdeau, R.W., Lee-Gosselin, A., Lakshmanan, A., Farhadi, A., Kumar, S.R., Nety, S.P., and Shapiro, M.G. (2018). Acoustic reporter genes for noninvasive imaging of microorganisms in mammalian hosts. Nature 553, 86–90.

Chamberland, S., Yang, H.H., Pan, M.M., Evans, S.W., Guan, S., Chavarha, M., Yang, Y., Salesse, C., Wu, H., Wu, J.C., et al. (2017). Fast two-photon imaging of subcellular voltage dynamics in neuronal tissue with genetically encoded indicators. Elife 27, https://doi.org/10.7554/eLife.25690.

Chen, T.W., Wardill, T.J., Sun, Y., Pulver, S.R., Renninger, S.L., Baohan, A., Schreiter, E.R., Kerr, R.A., Orger, M.B., Jayaraman, V., et al. (2013). Ultrasensitive fluorescent proteins for imaging neuronal activity. Nature 499, 295–300.

Deán-Ben, X.L., Sela, G., Lauri, A., Kneipp, M., Ntziachristos, V., Westmeyer, G.G., Shoham, S., and Razansky, D. (2016). Functional optoacoustic neuro-tomography for scalable whole-brain monitoring of calcium indicators. Light Sci. Appl. 5, e16201.

Deán-Ben, X.L., Gottschalk, S., Mc Larney, B., Shoham, S., and Razansky, D. (2017). Advanced optoacoustic methods for multiscale imaging of in vivo dynamics. Chem. Soc. Rev. 46, 2158–2198.

Estrada, H., Turner, J., Kneipp, M., and Razansky, D. (2014). Real-time optoacoustic brain microscopy with hybrid optical and acoustic resolution. Laser Phys. Lett. 11, 045601.

Fabritius, A., Ng, D., Kist, A.M., Erdogan, M., Portugues, R., and Griesbeck, O. (2018). Imaging-based screening platform assists protein engineering. Cell Chem. Biol. 25, 1554–1561.

Gangola, P., and Rosen, B.P. (1987). Maintenance of intracellular calcium in escherichia coli. J. Biol. Chem. 262, 12570–12574.

Gottschalk, S., Estrada, H., Degtyaruk, O., Rebling, J., Klymenko, O., Rosemann, M., and Razansky, D. (2015). Short and long-term phototoxicity in cells expressing genetic reporters under nanosecond laser exposure. Biomaterials 69, 38–44.

Gottschalk, S., Fehm, T.F., Deán-Ben, X.L., Tsytsarev, V., and Razansky, D. (2016). Correlation between volumetric oxygenation responses and electrophysiology identifies deep thalamocortical activity during epileptic seizures. Neurophotonics 4, 011007.

Gottschalk, S., Degtyaruk, O., Mc Larney, B., Rebling, J., Hutter, M.A., Deán-Ben, X.L., Shoham, S., and Razansky, D. (2019). Rapid volumetric optoacoustic imaging of neural dynamics across the mouse brain. Nat. Biomed. Eng. 3, 392–401.

Gozzi, A., and Schwarz, A.J. (2016). Large-scale functional connectivity networks in the rodent brain. NeuroImage 127, 496–509.

Helmchen, F., and Denk, W. (2005). Deep tissue two-photon microscopy. Nat. Methods 2, 932–940.

Ji, N., Freeman, J., and Smith, S.L. (2016). Technologies for imaging neural activity in large volumes. Nat. Neurosci. 19, 1154–1164.

Jonckers, E., Van Audekerke, J., De Visscher, G., Van der Linden, A., and Verhoye, M. (2011). Functional connectivity fMRI of the rodent brain: comparison of functional connectivity networks in rat and mouse. PLoS One 6, e18876.

Kannan, M., Vasan, G., Huang, C., Haziza, S., Li, J.Z., Inan, H., Schnitzer, M.J., and Pieribone, V.A. (2018). Fast, in vivo voltage imaging using a red fluorescent indicator. Nat. Methods 15, 1108–1116.

Laufer, J., Jathoul, A., Pule, M., and Beard, P. (2013). In vitro characterization of genetically expressed absorbing proteins using photoacoustic spectroscopy. Biomed. Opt. Express 4, 2477.

Li, Y., Forbrich, A., Wu, J., Shao, P., Campbell, R.E., and Zemp, R. (2016). Engineering dark chromoprotein reporters for photoacoustic microscopy and FRET imaging. Sci. Rep. 6, 22129.

Lyu, Y., Xie, C., Chechetka, S.A., Miyako, E., and Pu, K. (2016). Semiconducting polymer nanobioconjugates for targeted photothermal activation of neurons. J. Am. Chem. Soc. 138, 9049–9052.

Mank, M., Reiff, D.F., Heim, N., Friedrich, M.W., Borst, A., and Griesbeck, O. (2006). A FRET-based calcium biosensor with fast signal kinetics and high fluorescence change. Biophys. J. 90, 1790–1796.

Mihalcescu, I., Van-Melle Gateau, M., Chelli, B., Pinel, C., and Ravanat, J.L. (2015). Green autofluorescence, a double edged monitoring tool for bacterial growth and activity in micro-plates. Phys. Biol. 12, 066016.

Mittmann, W., Wallace, D.J., Czubayko, U., Herb, J.T., Schaefer, A.T., Looger, L.L., Denk, W., and Kerr, J.N. (2011). Two-photon calcium imaging of evoked activity from L5 somatosensory neurons in vivo. Nat. Neurosci. 14, 1089–1093.

Ni, R., Rudin, M., and Klohs, J. (2018). Cortical hypoperfusion and reduced cerebral metabolic rate of oxygen in the arcAß mouse model of Alzheimer's disease. Photoacoustics 10, 38–47.

Ohkura, M., Sasaki, T., Kobayashi, C., Ikegaya, Y., and Nakai, J. (2012). An improved genetically encoded red fluorescent Ca^{2+} indicator for detecting optically evoked action potentials. PLoS One 7, 1–7.

Patriarchi, T., Cho, J.R., Merten, K., Howe, M.W., Marley, A., Xiong, W.H., Folk, R.W., Broussard, G.J., Liang, R., Jang, M.J., et al. (2018). Ultrafast neuronal imaging of dopamine dynamics with designed genetically encoded sensors. Science 360, eaat4422.

Prevedel, R., Yoon, Y.G., Hoffmann, M., Pak, N., Wetzstein, G., Kato, S., Schrödel, T., Raskar, R., Zimmer, M., Boyden, E.S., and Vaziri, A. (2014). Simultaneous whole-animal 3D imaging of neuronal activity using light-field microscopy. Nat. Methods 11, 727–730.

Rao, B., Zhang, R., Li, L., Shao, J.Y., and Wang, L.V. (2017). Photoacoustic imaging of voltage responses beyond the optical diffusion limit. Sci. Rep. 7, 2560.

Rebling, J., Estrada, H., Gottschalk, S., Sela, G., Zwack, M., Wissmeyer, G., Ntziachristos, V., and Razansky, D. (2018). Dual-wavelength hybrid optoacoustic- ultrasound biomicroscopy for functional imaging of large-scale cerebral vascular networks. J. Biophoton. 11, e201800057.

Shen, Y., Dana, H., Abdelfattah, A.S., Patel, R., Shea, J., Molina, R.S., Rawal, B., Rancic, V., Chang, Y.F., Wu, L., et al. (2018). A genetically encoded Ca^{2+} indicator based on circularly permutated sea anemone red fluorescent protein eqFP578. BMC Biol. 16, 9.

Stirman, J.N., Smith, I.T., Kudenov, M.W., and Smith, S.L. (2016). Wide field-of-view, multi-region, two-photon imaging of neuronal activity in the mammalian brain. Nat. Biotechnol. 34, 857–862.

Sun, F., Zeng, J., Jing, M., Zhou, J., Feng, J., Owen, S.F., Luo, Y., Li, F., Wang, H., Yamaguchi, T., et al. (2018). A genetically encoded fluorescent sensor enables rapid and specific detection of dopamine in flies, fish, and mice. Cell 174, 481–496.

Thestrup, T., Litzlbauer, J., Bartholomäus, I., Mues, M., Russo, L., Dana, H., Kovalchuk, Y., Liang, Y., Kalamakis, G., Laukat, Y., et al. (2014). Optimized ratiometric calcium sensors for functional in vivo imaging of neurons and T lymphocytes. Nat. Methods 11, 175–182.

Wang, L.V. (2009). Multiscale photoacoustic microscopy and computed tomography. Nat. Photon. 3, 503–509.

Wang, X., Pang, Y., Ku, G., Xie, X., Stoica, G., and Wang, L.V. (2003). Noninvasive laser-induced photoacoustic tomography for structural and functional in vivo imaging of the brain. Nat. Biotechnol. 21, 803–806.

Weber, J., Beard, P.C., and Bohndiek, S.E. (2016). Contrast agents for molecular photoacoustic imaging. Nat. Methods 13, 639–650.

Yao, J., Wang, L., Yang, J.M., Maslov, K.I., Wong, T.T., Li, L., Huang, C.H., Zou, J., and Wang, L.V. (2015). High-speed label-free functional photoacoustic microscopy of mouse brain in action. Nat. Methods 12, 407–410.

Zhang, H.K., Yan, P., Kang, J., Abou, D.S., Le, H.N., Jha, A.K., Thorek, D.L., Kang, J.U., Rahmim, A., Wong, D.F., et al. (2017). Listening to membrane potential: photoacoustic voltage-sensitive dye recording. J. Biomed. Opt. 22, 045006.

Zhao, Y., Araki, S., Wu, J., Teramoto, T., Chang, Y.F., Nakano, M., Abdelfattah, A.S., Fujiwara, M., Ishihara, T., Nagai, T., and Campbell, R.E. (2011). An expanded palette of genetically encoded Ca^{2+} indicators. Science 333, 1888–1891.

Supplemental Information

High-Throughput Platform

for Optoacoustic Probing of Genetically

Encoded Calcium Ion Indicators

Urs A.T. Hofmann, Arne Fabritius, Johannes Rebling, Héctor Estrada, X. Luís Deán-Ben, Oliver Griesbeck, and Daniel Razansky

1 Transparent Methods

1.1 Optoacoustic microscope

Pulsed Optoacoustic (OA) excitation was achieved by a wavelength tunable dye laser (Credo, Sirah Lasertechnik, Germany) which was pumped by a 532 nm Nd:YAG laser (IS811-E, Edgewave, Germany) at up to 10 kHz. The use of Pyrromethene 597 (Sirah Lasertechnik, Germany) allowed wavelength tuning over a range of 558 nm to 587 nm, while alternative dyes enable excitation in the entire visible and NIR range. The dye laser was tuned to an output wavelength of 560 nm (0.15 nm bandwidth) corresponding to the peak absorption wavelength of R-GECO1 (Shen et al. 2018). A broadband $\lambda/2$-waveplate (AHWP10M-600, Thorlabs, USA) in combination with a polarizing beam splitter (PBS251, Thorlabs, USA) enabled accurate and seamless adjustment of the per-pulse-energy (PPE) of the laser in the 1 µJ to 150 µJ range. PPEs were measured using a high-speed laser power meter (J-10MT-10KHZ, Coherent, USA). During OA measurements, a beam sampler (BSF10-A, Thorlabs, Newton, USA) redirected 1 % of each laser pulse to a fast photodiode (PD; DET10A, Thorlabs, USA) to reduce measurement errors induced by PPE fluctuations (approx. 5 % for the used wavelengths and PPEs). The beam size was adapted using an iris (SMD1D12SS, Thorlabs, USA) and was then focused into an optical fiber by a 100 mm focal distance lens (AC254-100-A-ML, Thorlabs, USA). A six-dimensional adjustable stage (K6XS, Thorlabs, USA) allows translation and rotation of the fiber input among three axes to adjust its position and orientation for high coupling efficiency (typically 80 % to 90 %). The fiber output was positioned within the central hole of an ultrasound (US) transducer, thus co-aligning the fiber's optical and transducer's acoustic axis (Estrada et al. 2014; Rebling et al. 2018). The small fiber core diameter of 105 µm combined with its low numerical aperture of 0.1 resulted in a 708 µm diameter spot at the working distance of 6 mm (FG105LVA, Thorlabs, USA). The custom-made polyvinylidene difluoride (PVDF) US transducer had a focal distance of 6 mm and 6 mm aperture diameter (Precision Acoustics, UK). Lateral resolution of approximately 60 µm was achieved with the effective transducer bandwidth of 30 MHz. Two stages mounted perpendicular to each other scanned the transducer over the sample reaching a velocity of up to 500 mm s^{-1} at 5 m s^{-2} acceleration (DDSM50/M, Thorlabs, USA)

while covering a field of view (FOV) of 50 mm x 50 mm. A dedicated pre-amplification system amplified the US signals by 8 dB directly at the transducer output followed by a low noise, broadband 24 dB amplifier (ZFL-500LN, Mini-Circuits, USA). The signal was then digitized by a data acquisition card (DAC; M4I.4420-X8, Spectrum Systementwicklung Microelectronic, Germany) which simultaneously acquired photodiode (PD) signals at a sampling frequency of 250 MHz. For each sampling position, 2400 samples were acquired corresponding to an effective sound propagation distance of 14 mm. A personal computer (PC) running Windows 10 and MATLAB 2018a (MathWorks, USA) collected the data (64 Gb RAM, Intel Core i7-6800K). Postprocessing was performed using Python 3 and MATLAB.

1.2 Fluorescence widefield microscope

A widefield camera (UI-2240-SE-M-GL, IDS, Germany) positioned concentrically over the Petri dish imaged the samples. Excitation light was delivered coaxially from below using a fiber coupled Tungsten light source (OSL2, Thorlabs, USA) providing 150 W unfiltered, broadband light. Two filter wheels (CFW6/M, Thorlabs, UK) were positioned in front of fiber output and camera objective, respectively. For R-GECO1, the excitation light was bandpass filtered around (559 ± 34) nm (MF559-34 - TXRED, Thorlabs, USA) and the emission light around (630 ± 69) nm (MF630-69 TXRED, Thorlabs, USA). The light source was used at full power (150 W) since illumination was provided from below through the Whatman filter paper. Exposure time was set to 2 s as a trade-off between acquiring sufficient signal in calcium ion (Ca^{2+})-unloaded state and avoiding saturation in Ca^{2+}-loaded state without having to change the exposure settings. A motorized stage (MTS50/M-Z8, Thorlabs, USA) moved the Petri dish in vertical direction to switch between loading position, Fluorescence (FL) imaging, and OA imaging. Acquired widefield images were corrected for camera distortion and light refraction at the water surface.

1.3 Scan procedure

Three-dimensional OA images were acquired in a mechanical overfly scan: a fast stage moved the transducer back and forth between scan window boundaries while the slow stage moved incrementally

after each line scan, resulting in an overall meander pattern. The slow stage carries a significantly higher mass (660 g) than the fast stage (30 g). Thus, scanning the full FOV containing 250 thousand sampled positions typically lasted 150 s using $5\,\mathrm{m\,s^{-2}}$ and $0.8\,\mathrm{m\,s^{-2}}$ acceleration for fast and slow stage respectively.

Triggering of the laser pulses and the subsequent digitization were based on the continuous position readings of the fast-moving stage. In this way, the sample was interrogated at an equally spaced grid of points regardless of stage acceleration and velocity. A microcontroller (Teensy 3.6, PJRC, USA) read out the x-stage quadrature encoder signal which provided a position accuracy of 500 nm. The laser and DAC were then triggered after a stage movement of 100 µm in both directions. For each scanning position, the data acquisition card (DAC) trigger was delayed by 106 µs to account for the laser delay. Due to position dependent triggering, no oversampling and excessive sample illumination occurred during acceleration and deceleration phases, further leading to optimization of the data size.

In order to accurately quantify performance of the protein variant expressed by a bacterial colony, we delivered a laser PPE of only 25 µJ (fluence of $6.54\,\mathrm{mJ\,cm^{-2}}$, 10 nm pulse duration) through a multimode optical fiber (NA 0.1, 105 µm core diameter) to obtain a single-shot signal-to-noise ratio (SNR) higher than 20 dB. Since the scan step size was smaller than the illumination spot diameter (approx. 700 µm), each position was illuminated multiple times during a single scan resulting in an accumulated energy density of $62.5\,\mathrm{mJ\,cm^{-2}}$.

1.4 Signal processing

Each recorded US signal was bandpass filtered between 0.5 MHz to 15 MHz, which reduced random noise and low frequency bias in the signals. To compensate for laser energy fluctuations, PPEs of shots were calculated based on the integrated PD signal and then used to normalize the measured US signals. The envelope of the filtered and corrected dataset was used to extract the OA signal intensity. For visualization, maximum intensity projections were calculated for the volumetric datasets. To reduce post-scan processing time, bandpass filtering, envelope extraction, PD correction, and maximum intensity projection calculation are performed during the scan. While the stages scan line i, post-

processing is simultaneously performed for line $i - 1$. In this way, all the acquired data can be pre-processed and stored in memory during the scan.

1.5 Probing

Cell colonies were individually probed based on OA or FL images. To coregister coordinate systems of the two modalities, checkerboard phantoms were imaged. The FL image is then cropped, scaled, and rotated until it matches the OA image. For localizing the colonies, circular shapes were detected using the Hough transformation in either OA or FL images, resulting in a set of n center points (Yuen et al. 1990). A $n \times n$ cost matrix was calculated describing the time required to travel between distinct positions taking into account different achievable accelerations of the stages. The so called traveling salesman problem was solved using a genetic optimization algorithm (Beardwood, Halton, and Hammersley 1959; Ulder et al. 1991). After the approximate optimum trajectory was estimated, cells were probed individually. The optimized path can be used to probe the extracted positions over multiple timepoints or wavelengths as long as the Petri dish is kept in place.

1.6 Biological samples

Most genetically encoded calcium ion indicators (GECIs) were tailored towards a high relative change in their brightness upon Ca^{2+} delivery which is given by

$$\frac{\Delta F}{F_{min}} = \frac{\sigma_a \cdot \epsilon_a - \sigma_b \cdot \epsilon_b}{\sigma_b \cdot \epsilon_b} \tag{1}$$

where $\sigma_{a,b}$ quantum yield after / before binding to Ca^{2+}

$\epsilon_{a,b}$ extinction coefficient after / before binding to Ca^{2+}.

OA signal intensity is proportional to $(1 - \sigma) \cdot \epsilon$ hence the maximum relative increase is defined via

$$\frac{\Delta OA}{OA_{min}} = \frac{(1 - \sigma_a) \cdot \epsilon_a - (1 - \sigma_b) \cdot \epsilon_b}{(1 - \sigma_b) \cdot \epsilon_b}. \tag{2}$$

An increase in σ is thus related to a decrease in OA intensity. To select an appropriate starting point for screenings, several existing GECIs were compared (see Supplementary Material 2). R-GECO1 was identified as a promising variant and used to showcase probing functionality of the platform. The genetically encoded Ca^{2+} indicator R-GECO1 was *de novo* synthesized (GeneArt Strings, Thermo Fisher Scientific, Germany) and cloned into a modified variant of pRSETB (Invitrogen, USA) using SLiCe cloning (Zhang, Werling, and Edelmann 2012; Zhao et al. 2011). For imaging experiments purified plasmid was transformed into *E. coli* XL1 blue (Stratagene, USA) and plated on Lysogeny broth agar containing $100\,\mu g\,mL^{-1}$ ampicillin (Carl Roth, Germany) to a density of approximately 500 to 800 colonies per Petri dish. Bacterial colonies were grown overnight at $37\,°C$ to a size of $0.5\,mm$ to $1\,mm$ and subsequently incubated at $4\,°C$ for $24\,h$ to fully mature expressed sensors (Litzlbauer et al. 2015). Individual colonies rarely overlapped or fused which allowed us to distinguish between signals originating from different colonies. Ca^{2+} was delivered as previously described (Litzlbauer et al. 2015). Prior to imaging, the cells were transferred onto a Whatman filter paper which is subsequently placed within a new Petri dish. To keep colonies in place, the paper was covered with a thin Agar layer. For good acoustic coupling $30\,mL$ of buffer were added to the Petri dish. After OA and FL imaging of the Ca^{2+} unbound state, Ca^{2+} was added to a concentration of $50\,mmol\,dm^{-3}$.

1.7 Optoacoustic and optical absorption spectrum of purified protein

Protein isolation and purification was performed as follows. His-tagged GECIs were recombinantly expressed at $37\,°C$ overnight in $50\,mL$ modified autoinduction medium in *E. coli* BL21 (DE3). Cells were harvested through centrifugation (5000 xg, $10\,min$, $4\,°C$) and resuspended in a $10\,mL$ resuspension buffer ($20\,mmol\,dm^{-3}$ imidazole, Merck, Germany; $300\,mmol\,dm^{-3}$ NaCl, Merck, Germany; $20\,mmol\,dm^{-3}$ Na2HPO4, Merck, Germany; pH 7.8) supplemented with a protease inhibitor cocktail ($4\,mmol\,dm^{-3}$ PMSF, Sigma Aldrich, Germany; $20\,\mu g\,mL^{-1}$ Pepstatin A, Sigma Aldrich, Germany; $4\,\mu g\,mL^{-1}$ Leupeptin, Sigma Aldrich, Germany). Cells were lysed through sonication using a Bandelin Sonopuls ($7\,min$, $80\,\%$ cycle, $80\,\%$ power). After lysis, the insoluble components were pelleted (18000 xg, $30\,min$, $4\,°C$). The supernatant was incubated with $150\,\mu L$ of Ni-IDA agarose

beads (Jena Bioscience, Germany) overnight at 4 °C with light agitation. Beads were collected in gravity flow columns (Qiagen, Germany) and washed with 10 mL wash buffer (55 mmol dm^{-3} imidazole, 300 mmol dm^{-3} NaCl, 20 mmol dm^{-3} Na2HPO4, pH 7.8). Finally, proteins were eluted in 800 µL elution buffer (250 mmol dm^{-3} imidazole, 300 mmol dm^{-3} NaCl, 20 mmol dm^{-3} Na2HPO4, pH 7.8).

1 mmol dm^{-3} Ca^{2+} (stock solution 250 mmol dm^{-3}, Calcium chloride dihydrate, Honeywell, USA) was added to three batches containing 500 µL of the purified protein each to switch the protein into Ca^{2+}-bound state. Each batch was then divided into two 250 µL aliquots and 5 mmol dm^{-3} EDTA (stock solution 500 mmol dm^{-3}, Ethylenediaminetetraacetic acid, Sigma-Aldrich, Germany) was added to one of them to remove Ca^{2+} from the protein and revert it into the unbound state.

The OA spectrum was measured by injecting the aliquots in a polyethylene tubing (0.58 mm and 0.96 mm inner and outer diameters, respectively, Smiths Medical Inc. Minneapolis, USA) embedded in agar. The generated OA signals were collected with a custom-made 256-element spherical array (4 MHz central detection frequency, 100 % detection bandwidth, 40 mm radius and 90° angular aperture, Imasonic SaS, Voray, France) (Deán-Ben and Razansky 2013). Three-dimensional images were formed with a 3D back-projection algorithm that effectively averages the signals from the individual transducers, thus resulting in an enhanced SNR of the OA readings. Excitation was performed with a tunable optical parametric oscillator (OPO)-based laser (Innolas GmbH, Krailling, Germany). The laser beam was guided via a custom-made fiber bundle (CeramOptec GmbH, Bonn, Germany) to illuminate the tubing with optical fluence of 10 mJ cm^{-2}. The laser wavelength was tuned from 415 nm to 680 nm in 5 nm steps on a per-pulse basis. Acquisition was performed for 50 wavelength cycles and the images corresponding to each wavelength were averaged after reconstruction. No significant bleaching was observed by comparing the individual frames. The measured OA spectrum was normalized with the wavelength-dependent laser energy per pulse, which was estimated by injecting a black India ink solution (optical density 1, Higgins-Chartpak Inc. Leeds, USA) and comparing the OA readings with the ink spectrum measured with a spectrophotometer (Ocean Optics Inc. Largo, USA). The optical absorption spectrum of the purified protein was additionally measured in both Ca^{2+} loaded and unloaded state between 400 nm to 700 nm at 1 nm step size using a photospectrometer (Cary 100, Varian,

US).

1.8 Viability of bacteria after screening

To prove viability of bacterial colonies after imaging using pulsed laser irradiation, a plate containing R-GECO1 expressing *Escherichia coli* (*E.Coli*) colonies was further imaged at high PPE (50 µJ at 560 nm) before and after Ca^{2+} delivery following the described procedure. Afterwards, a colony providing good optoacoustic signal was picked, mechanically resuspended in buffer solution, and sprayed on a fresh agar plate. The plate was incubated overnight and checked for growth of bacterial colonies the following morning.

All code used for hardware control and evaluation of the datasets are available online: https://github.com/razanskylab/.

2 Comparison of existing sensor proteins for optoacoustic imaging

Table S1: Comparison of different red-shifted GECIs developed for FL monitoring of Ca^{2+} dynamics in the mammalian brain. λ_{ex} - excitation wavelength, σ - quantum yield, ϵ - extinction coefficient, FL - fluorescent brightness, OA_b - OA brightness, $\Delta FL/FL_{min}$ - relative fluorescence change upon Ca^{2+} delivery, $\Delta OA/OA_{min}$ - relative optoacoustic change upon Ca^{2+} delivery. [*] denotes $\frac{1}{mM\ cm}$. Related to Fig. 3.

Protein	λ_{ex} [nm]	σ_b [1]	ϵ_b [*]	FL_b [*]	OA_b [*]	σ_a [1]	ϵ_a [*]	FL_a [*]	OA_a [*]	$\frac{\Delta FL}{FL_{min}}$ [%]	$\frac{\Delta OA}{OA_{min}}$ [%]
K-GECO1(Shen et al. 2018)	568	0.12	19	2.28	17	0.45	61	27.45	34	1104	101
R-GECO1(Zhao et al. 2011)	577	0.06	15	0.90	14	0.20	51	10.20	41	1033	189
RCaMP1a(Akerboom et al. 2013)	577	0.12	35	4.18	31	0.45	57	25.52	31	511	2
RCaMP1c(Akerboom et al. 2013)	577	0.10	40	3.97	36	0.48	65	31.10	34	683	-6
RCaMP1d(Akerboom et al. 2013)	572	0.13	25	3.30	22	0.52	58	30.06	28	810	26
RCaMP1f(Akerboom et al. 2013)	572	0.11	17	1.91	15	0.48	59	28.27	31	1377	98
RCaMP1h(Akerboom et al. 2013)	571	0.14	19	2.62	16	0.51	65	33.20	32	1168	98
RCaMP1.07(Ohkura et al. 2012)	562	0.11	14	1.56	13	0.23	48	11.06	37	608	624
RCaMP2(Inoue et al. 2014)	563	0.11	14	1.56	13	0.23	48	11.06	37	608	193

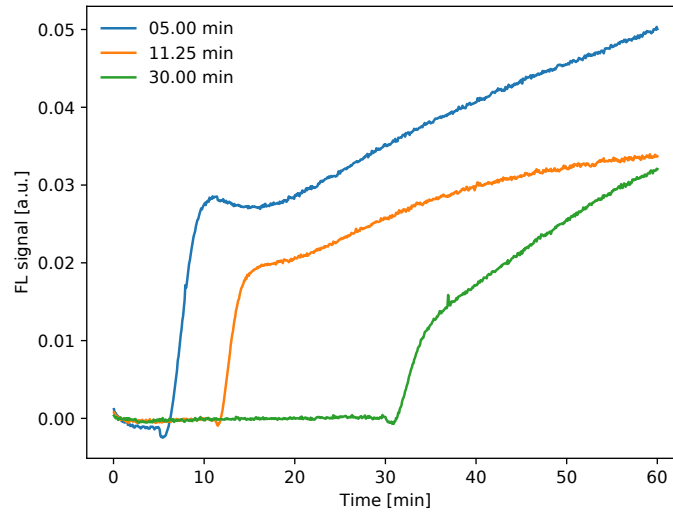# 3 Influence of delivery time onto calcium ion uptake dynamics

Figure S1: Influence of time between taking plates out of fridge and delivering Ca^{2+} on FL signal intensity: beside the time after Ca^{2+} delivery to the buffer medium, also the time after taking them from a cold fridge (7 °C) into a warm environment influences the dynamic behaviour of the protein response. If Ca^{2+} is delivered shortly after taking the colonies out of the fridge, the response occurs in general faster compared to long waiting times. All experiments within this paper were performed on plates just taken out of the fridge, related to Fig. 4C.

References

Shen, Yi et al. (Jan. 2018). "A genetically encoded Ca^{2+} indicator based on circularly permutated sea anemone red fluorescent protein eqFP578". In: *BMC Biology* 16.9. DOI: 10.1186/s12915-018-0480-0.

Estrada, Héctor, Jake Turner, Moritz Kneipp, and Daniel Razansky (Feb. 2014). "Real-time optoacoustic brain microscopy with hybrid optical and acoustic resolution". In: *Laser Physics Letters* 11.4, p. 045601. DOI: 10.1088/1612-2011/11/4/045601.

Rebling, Johannes, Héctor Estrada, Sven Gottschalk, Gali Sela, Michael Zwack, Georg Wissmeyer, Vasilis Ntziachristos, and Daniel Razansky (May 2018). "Dual-wavelength hybrid optoacoustic-ultrasound biomicroscopy for functional imaging of large-scale cerebral vascular networks". In: *Journal of Biophotonics* 11.9, e201800057. DOI: 10.1002/jbio.201800057.

Yuen, HK, J Princen, J Illingworth, and J Kittler (Feb. 1990). "Comparative study of Hough Transform methods for circle finding". In: *Image and Vision Computing* 8.1, pp. 71–77. DOI: 10.1016/0262-8856(90)90059-e.

Beardwood, Jillian, J. H. Halton, and J. M. Hammersley (Oct. 1959). "The shortest path through many points". In: *Mathematical Proceedings of the Cambridge Philosophical Society* 55.4, pp. 299–327. DOI: 10.1017/s0305004100034095.

Ulder, Nico L. J., Emile H. L. Aarts, Hans-Jürgen Bandelt, Peter J. M. van Laarhoven, and Erwin Pesch (1991). "Genetic local search algorithms for the traveling salesman problem". In: *Parallel Problem Solving from Nature*. Ed. by Hans-Paul Schwefel and Reinhard Männer. Berlin, Heidelberg: Springer Berlin Heidelberg, pp. 109–116. ISBN: 978-3-540-70652-6.

Zhang, Yongwei, Uwe Werling, and Winfried Edelmann (Jan. 2012). "SLiCE: a novel bacterial cell extract-based DNA cloning method". In: *Nucleic Acids Research* 40.8, e55–e55. DOI: 10.1093/nar/gkr1288.

Zhao, Y. et al. (Sept. 2011). "An Expanded Palette of Genetically Encoded Ca^{2+} Indicators". In: *Science* 333.6051, pp. 1888–1891. DOI: 10.1126/science.1208592.

Litzlbauer, Julia, Martina Schifferer, David Ng, Arne Fabritius, Thomas Thestrup, and Oliver Griesbeck (June 2015). "Large Scale Bacterial Colony Screening of Diversified FRET Biosensors". In: *PLOS ONE* 10.6. Ed. by Sabato D'Auria, e0119860. DOI: 10.1371/journal.pone.0119860.

Deán-Ben, X. Luís and Daniel Razansky (Nov. 2013). "Portable spherical array probe for volumetric real-time optoacoustic imaging at centimeter-scale depths". In: *Optics Express* 21.23, p. 28062. DOI: 10.1364/oe.21.028062.

Akerboom, Jasper et al. (Mar. 2013). "Genetically encoded calcium indicators for multi-color neural activity imaging and combination with optogenetics". In: *frontiers in Molecular Neuroscience* 6.2, pp. 1–29. DOI: 10.3389/fnmol.2013.00002.

Ohkura, Masamichi, Takuya Sasaki, Chiaki Kobayashi, Yuji Ikegaya, and Junichi Nakai (July 2012). "An Improved Genetically Encoded Red Fluorescent Ca^{2+} Indicator for Detecting Optically Evoked Action Potentials". In: *PLoS One* 7.7, pp. 1–7. DOI: 10.1371/journal.pone.0039933.

Inoue, Masatoshi et al. (Nov. 2014). "Rational design of a high-affinity, fast, red calcium indicator R-CaMP2". In: *Nature Methods* 12, pp. 64–70. DOI: 10.1038/nmeth.3185.